Engineering 15 (2022) 196–205

Contents lists available at ScienceDirect

Engineering

journal homepage: www.elsevier.com/locate/eng

Research
3D Printing, Flexible Sensor, Superhydrophobic, Magnetic—Article

3D-Printed Superhydrophobic and Magnetic Device That Can Self-Powered Sense A Tiny Droplet Impact

Xuan Zhang [a,c], Qi Wang [b], Ruiping Zou [c], Bo Song [a], Chunze Yan [a], Yusheng Shi [a], Bin Su [a,*]

[a] State Key Laboratory of Material Processing and Die & Mould Technology, School of Materials Science and Engineering, Huazhong University of Science and Technology, Wuhan 430074, China
[b] State Key Laboratory of Advanced Electromagnetic Engineering and Technology, School of Electrical and Electronic Engineering, Huazhong University of Science and Technology, Wuhan 430074, China
[c] ARC Research Hub for Computational Particle Technology, Department of Chemical Engineering, Monash University, Clayton VIC 3800, Australia

ARTICLE INFO

Article history:
Received 6 September 2021
Revised 10 March 2022
Accepted 20 April 2022
Available online 14 May 2022

Keywords:
3D printing
Self-powered sensing
Magnetic
Waterdrops

ABSTRACT

Three-dimensional (3D)-printed magnetic soft architectures have attracted extensive attention and research from the engineering and material fields. The force-driven shape deformation of such architectures causes a change in the magnetic field distribution, indicating the capability to convert mechanical energy to electricity. Herein, we fabricate a flexible superhydrophobic and magnetic device by integrating two kinds of 3D printing approaches. The 3D-printed magnetic device (3DMD) exhibits a long-term stable mechanoelectrical conversion capacity under consecutive water droplet dripping. The output current of the 3DMD is higher than that of records in the existing literature. Combined with Maxwell numerical simulation, the mechanoelectrical conversion mechanism of the 3DMD is investigated, further guiding regulation of the diverse parameters. Moreover, three 3DMDs are integrated to light up a commercial light-emitting diode (LED) by a stream of collected rainwater. Such a combined design incorporating energy conversion is believed to promisingly motive advances in the 3D printing field.

1. Introduction

Three-dimensional (3D) printing, as an emerging additive manufacturing technology, facilitates manufacturing of versatile and sophisticated structural prototypes, which demonstrates tremendous prospects in the discipline areas of aeronautical and space technologies, tissue engineering, jewellery, and flexible electronics [1–7]. Currently, 3D-printed magnetic architectures, which are composed of magnetic particles and printable polymers, are attracting tremendous interest due to their potential in controllable manipulators [8,9], shape deformable soft robots [10,11], and others [12–15]. Ji et al. [16] reported a soft gripper-type magnetic actuator by dual-material 3D printing in a one-step process (digital light processing (DLP)), allowing for deformation and object capture, transportation, and release under external magnetic actuation. Afterwards, Kim et al. [17] and Qi et al. [18] developed programmed ferromagnetic domains by direct ink writing (DIW) printing and fused deposition modelling (FDM) printing, respectively. They both applied a magnetic field during solidification in a polymer matrix, generating anisotropic magnetization profiles for magnetoactive soft materials. In contrast to liquid-based 3D printing approaches, selective laser sintering (SLS) printing was indicated to prepare magnetic-driven grippers for controllable deformation through magnetic stimuli [19].

In addition to serving as manipulators or soft robots driven by an external magnetic field [8–15], magnetic soft architectures exhibit a changed magnetic field distribution when they are deformed by applied forces, indicating the capability to convert mechanical energy to electricity. Recently, our group reported the concept of generating electricity from waterdrops by a flexible magnetic system [20]. However, several parts of the setup are moulded and then assembled, indicating a tedious and time-consuming fabrication process. 3D printing approaches are reasonably believed to facilitate manufacturing of magnetic energy harvesters. Furthermore, the 3D printing process enables easy tuning of the magnetic structures based on digital design and manufacturing. In this case, diverse magnetic architectures can be generated, allowing for optimized design for the maximum electrical output.

Herein, we utilize 3D printing approaches to fabricate a flexible magnetic device with a superhydrophobic surface, enabling

* Corresponding author.
E-mail address: subin@hust.edu.cn (B. Su).

https://doi.org/10.1016/j.eng.2022.04.009

mechanoelectrical conversion driven by waterdrops. The flexible mechanoelectrical conversion device is composed of a magnetic top and an elastic stem-like bottom, which were fabricated by two types of 3D printing processes. When suffering from the mechanical impact brought by a falling waterdrop, this 3D-printed magnetic device (3DMD) gives rise to a magnetic flux change through its inside conductive coil, accordingly generating electricity. Notably, the superhydrophobic feature of the magnetic top effectively diminishes the solid/liquid adhesion of water droplets, guaranteeing good elastic recovery of the device. In addition, controllable factors including fabrication and test parameters were tailored to investigate their effects on the electrical output performance, in combination with Maxwell numerical simulation. Finally, three 3DMDs were integrated in parallel into a cluster architecture setup, triggering lighting of a red light-emitting diode (LED) by a stream of collected rainwater. This study provides a new avenue for the fabrication of mechano-electrical conversion devices to achieve self-powered sensing systems.

2. Materials and methods

2.1. Materials

$Nd_2Fe_{14}B$ grains (400-mesh, Guangzhou Xinnuode Transmission Parts Co., Ltd., China), thermoplastic polyurethane (TPU) powders (LUVOSINT TPU X92A-2 WT, LEHVOSS Group, Germany), hydrophobic silica (AEROSIL R202, Evonik Degussa Co., Germany), ethanol (AR, $\geq$ 99.7%, Aladdin, China), and a photopolymer (Agilus30, Stratasys Ltd., USA) were purchased and used as received. Ring-shaped copper coils were purchased and customized with the following parameters: a wire diameter of 0.1 mm, an inner (outer) diameter of 3.2 mm (25 mm), and a thickness of 1.5 mm.

2.2. Fabrication of 3DMDs

Initially, $Nd_2Fe_{14}B$ magnetic powders were homogeneously mixed with TPU powders according to different mass ratios (20 wt%, 30 wt%, and 40 wt%) by ball-milling treatment. After sufficient mixing, the powdery composites were poured into an extrusion-moulding system including a single screw extruder and a thread roller (Wellzoom B, Shenzhen Mistar Technology Co., Ltd., China) to prepare flexible $Nd_2Fe_{14}B$-TPU composite filaments for 3D printing. To ensure efficient extrusion of required filaments, the extrusion temperature for the $Nd_2Fe_{14}B$-TPU composites was within a range of 140–160 °C based on the diverse mass ratios. Notably, temperatures exceeding 160 °C might result in degradation and even carbonization of the composites, as well as flowability and process stability issues. Meanwhile, a thread roller was used to collect $Nd_2Fe_{14}B$-TPU composite filaments. Then, the collected filaments were directly fed to an FDM 3D printer without second mixing to fabricate the magnetic top.

The structure of the 3DMDs in this work was designed via commercial 3ds Max software. Following an FDM 3D printing technique, diverse magnetic tops varying in thickness (1–3 mm) and papillary size (radius of 1.0 or 1.5 mm) were fabricated. The magnetic particles in the top were vertically magnetized by a pulsed magnetic field created by a magnetizer (JIUJU Industrial Equipment (HK) Co., Ltd., China) under a high voltage of more than 1900 V. Hydrophobic silica nanoparticles were dispersed in ethanol at a ratio of 10 wt% and sonicated before use. Then, the silica-based solution was sprayed onto the 3D-printed magnetic top for hydrophobic treatment. The Agilus30 photopolymer was employed to fabricate elastic stem-like supports via a Polyjet 3D printing technique, with different stem lengths from 2 to 8 mm. Finally, a 3DMD was fabricated through simple assembly of three components: a magnetic top, an elastic stem-like bottom, and a conductive copper coil.

2.3. Characterization and measurement

The dispersion of $Nd_2Fe_{14}B$ particles in composite-based magnetic filaments was observed by *in situ* X-ray micro-computed tomography (micro-CT) technology (Xradia 510 Versa, Zeiss, Germany). The morphology of $Nd_2Fe_{14}B$ particles, as well as the surface of the silica-treated/untreated magnetic top, were observed by field emission scanning electron microscopy (FESEM) (Sirion 200, FEI Company, USA). An ultradepth 3D microscope (DSX510, Olympus Co., Japan) was used to observe the papillary size on the magnetic top. The magnetic strength distribution of the printed top was determined by a multidimensional magnetic field test system (F-30, CH-Magnetoelectricity Technology, China). The contact angle of water on the silica-treated/untreated samples in the static mode was measured by a contact angle meter (SDC-350, Dongguan SINDIN Precision Instrument Co., Ltd., China). A high-speed camera system (ST-857, NAC Image Technology Inc., Japan) recorded the sample status in real time when a waterdrop dripped. Meanwhile, the relevant electrical responses to mechanical deformation due to vibration were investigated by an electrochemistry workstation (Autolab PGSTAT204, Metrohm, Switzerland).

2.4. Numerical simulation

ANSYS Maxwell analysis software was used to calculate the 3D magnetic strength distribution of different magnetic devices. The magnetization direction was fixed along the positive *z*-axis. An equivalent unary model was used according to our previous publications [21,22]. In this case, the model of the $Nd_2Fe_{14}B$-TPU magnetic top was set as a magnet of the same scale. In the simplified equivalent model, the magnetic coercivity (H_c) was -151197.2 $A{\cdot}m^{-1}$, while the residual magnetism (B_r) was 0.19 T.

3. Results

We constructed a 3DMD composed of a magnetic top and an elastic bottom, which were generated by FDM and Polyjet 3D printing techniques, respectively (Fig. 1). Generally, $Nd_2Fe_{14}B$ is deemed to be the strongest permanent-magnet material due to its high maximum energy product. Regarding low Young's modulus thermoplastic polymers, TPU is more suitable for building flexible architectures during FDM printing (Fig. S1 in Appendix A) [23–25]. Thus, $Nd_2Fe_{14}B$ powders with an average grain size of 18.95 μm (Fig. S2 in Appendix A) were homogeneously mixed with TPU powders in a 4:6 mass ratio (Fig. 1(a)), yielding magnetic filaments with excellent flexibility (Figs. 1(b), (f), and (g)) through an extrusion-moulding system (Fig. S3 in Appendix A).

Fig. 1(e) and Fig. S4 in Appendix A show the homogeneous dispersion of $Nd_2Fe_{14}B$ magnetic grains (light areas) inside a composite filament obtained by the *in situ* X-ray micro-CT technique. The single magnetic filament diameter is approximately 1.72 mm, which is beneficial for the FDM 3D printing equipment (Fig. 1(c) and Fig. S3(c) in Appendix A). Therefore, a 30 mm (diameter) × 3 mm (thickness) magnetic and superhydrophobic top (Figs. 1(d) and (h)) was printed after depositing a thin layer of hydrophobic silica fumed nanoparticles onto the magnetic top.

Then, a Polyjet 3D printing technique was used to fabricate a 30 mm (diameter) × 6 mm (length) stem-like elastic bottom (Figs. 1(i)–(k)). In contrast to the FDM technique, the Polyjet 3D

printing approach can manufacture low-Young's-modulus elastic polymers, providing a flexible support that can reversibly deform under an applied force. Last, the magnetic top and the flexible stem-like bottom were integrated by a commercial adhesive, yielding a 3DMD after inserting the coil in the bottom space (Fig. 1(l) and Fig. S5 in Appendix A).

The appearance and properties of the 3D-printed magnetic top were carefully investigated (Fig. 2). According to the optical image in Fig. 2(a), papillate structures were printed on the top surface. Since a thin layer of hydrophobic silica nanoparticles exists, the top is slightly white. Fig. 2(b) characterizes the quasi-hemispherical morphology of the papilla array on the magnetic top. A papillary height of approximately 0.92 mm was measured by an ultradepth 3D microscope (Fig. 2(e)). According to the magnified FESEM image (Fig. 2(c)), numerous silica nanoparticles aggregate. The low surface energy of the hydrophobic silica nanoparticles, combined with millimetre/nanoscale roughness, allows the printed top to show a superhydrophobic state (Fig. 2(f)) towards water.

In addition to the superhydrophobicity, the magnetic property of the printed top was investigated. After the magnetization treatment, the 3D distribution of the magnetic strength of the printed magnetic top was measured (Fig. 2(d)). Obviously, the strongest magnetic strength appears on the top of the papillae. The average surface magnetic intensity was ~9 mT.

The mechanoelectricalmechanoelectrical conversion of a 3DMD was studied (Fig. 3). The thickness, magnetic powder content of the printed top, and height of the elastic stem were 2 mm, 40 wt%, and 6 mm, respectively. Waterdrops (each droplet of 55 μL) were dripped onto the 3DMD surface with a release height of 40 cm. Since the stem-shaped bottom was printed by a low-Young's-modulus elastic polymer, the elastic stem could be sensitively bent and then recover, achieving a distance change between the magnetic top and the coil at the bottom part. In this case, the magnetic flux through the coil was changed, leading to electricity generation from the falling drop (Fig. 3(a)).

Snapshots recorded by a high-speed camera (Fig. 3(b)) exhibit the corresponding deformation processes. A distance change of approximately 1 mm between the magnetic top and the bottom coil can be found, allowing for a change of the magnetic flux through the coil. Therefore, the corresponding voltage and current outputs over time were recorded, as shown in Figs. 3(e) and (f), respectively, when a series of waterdrops dripped under the same parameters. Regular upwards–downwards response peaks can be found, in which the average outputs of the first voltage and current peaks reach 1.6 mV and 12.9 μA, respectively. The corresponding charge transferred during the deformation/recovery process is 5.2 μC (Fig. 3(g)). Generally, 3D-printed tactile sensors in previous studies [26,27] had to be powered by an external energy supply. Then, the self-powered concept, by using piezoelectric or triboelectric materials, was proposed to harvest the mechanical energy of water drops or tiny vibrations. Compared to the existing literature [28–35], the output current of our 3DMD is higher than the published records (Table 1 [26–35]) due to the electromagnetic working mechanism. In this case, the 3DMD can convert the gravitational potential energy of water droplets to electricity, showing a self-powered sensing capability [36–43].

Maxwell numerical simulations for the 3DMD before and after deformation were conducted to investigate the mechanoelectrical conversion mechanism. A 3D static magnetic solver was employed for 3D simulation modelling of the magnetic top to calculate the magnetic field distributions before and after deformation (Fig. 3(c)). In this case, an equivalent unary model was used [44,45] for simplification of the complex binary magnetic powder/polymer system. Fig. 3(d) shows the magnetic flux through one turn of the coil before/after the 3DMD deformation driven by

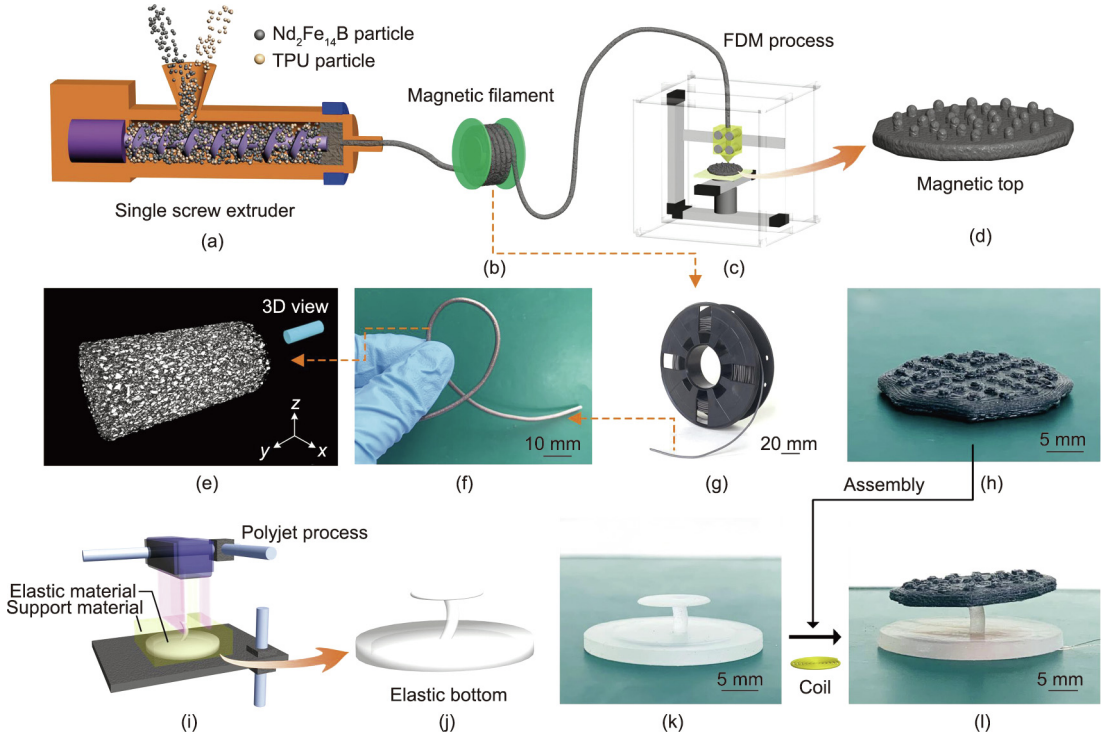

Fig. 1. Fabrication of the bioinspired 3DMD. (a)–(d) Schematic illustration of the manufacturing process of the magnetic top via FDM technology; (e)–(g) characterization of the composite-based magnetic filaments: (e) 3D image obtained by the micro-CT technique, optical photographs of (f) a single flexible magnetic filament, and (g) a reel of as-prepared magnetic filaments; (h) a printed magnetic top based on $Nd_2Fe_{14}B$ and TPU composite powders; (i, j) schematic illustrations of the manufacturing of the elastic component via Polyjet technology; (k) optical photographs of an elastic stem-like support; (l) a 3DMD assembled by a magnetic top, a conductive coil, and an elastic stem-like bottom.

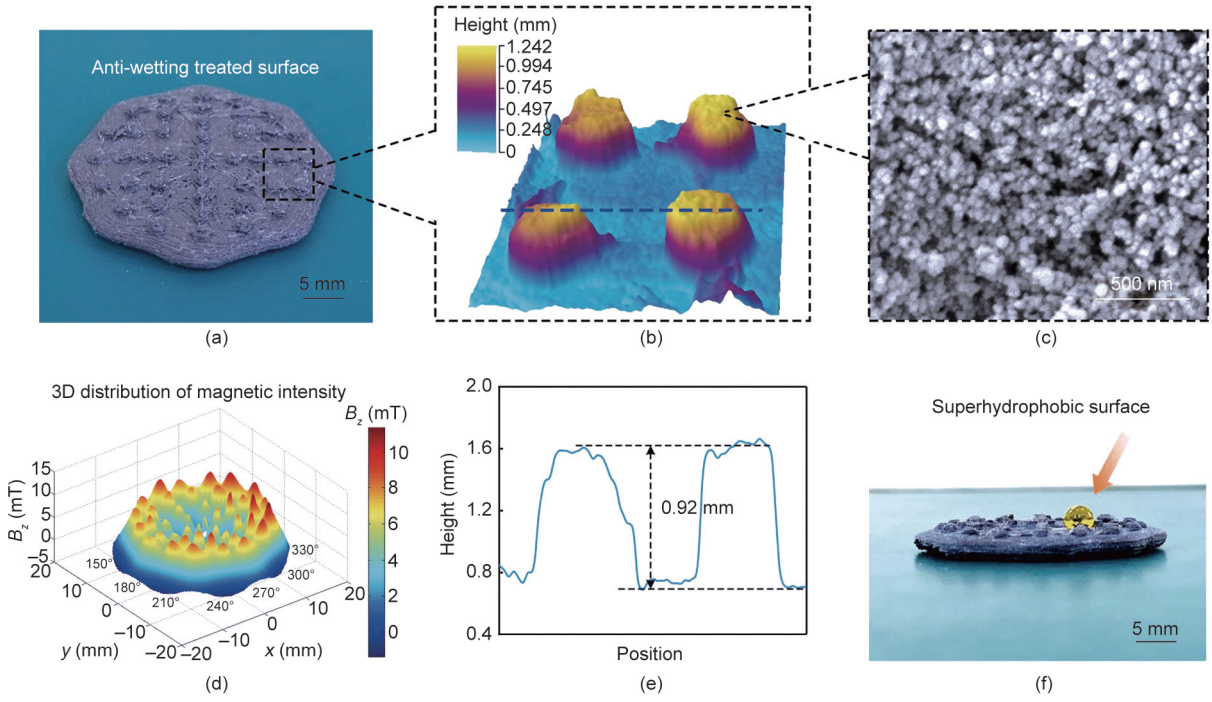

Fig. 2. Characterization of the superhydrophobic and magnetic top printed by the FDM technique. (a) Optical photograph of the superhydrophobic and magnetic top; (b) ultradepth 3D microscope image of the surface papillae; (c) FESEM image of hydrophobic silica nanoparticles on the treated surface of the magnetic top; (d) 3D distribution of the magnetic intensity of the silica-treated magnetic top, B_z is the magnetic strength in *z*-axis; (e) the papillary height measured by an ultradepth 3D microscope; (f) optical photograph showing the superhydrophobicity of the magnetic top towards a yellow-coloured water droplet.

waterdrop dripping, where the colour gradient (blue to red) represents a gradual increase in the magnetic field. The magnetic flux change can be found in Table S1 in Appendix A (a detailed calculation is shown in Note S1 in Appendix A). Thus, the gravitational potential energy of the released waterdrop can be transformed into the deformation of the 3DMD, yielding an increased magnetic flux in the 3DMD and thereby electricity generation.

To verify the significance of the superhydrophobic feature, an untreated 3DMD was prepared as a control sample, in which the components remained the same except for the superhydrophobic surface. The surfaces of these two samples can be found in Figs. S6(a) and (b) in Appendix A, respectively. Owing to the lower surface energy after silica treatment, the static water contact angle on the treated surface is approximately 151°, while it is only 62° on the untreated counterpart (Figs. S6(c) and (d) in Appendix A). Fig. 4 shows the electrical performance of superhydrophobic and hydrophilic 3DMDs under continuous dripping of waterdrops. When numerous water droplets were consecutively released from the same height onto these two systems, waterdrops rarely remained on the surface of the superhydrophobic system due to the anti-wetting property (Figs. 4(a) and (b)), whereas several water spots attached to the hydrophilic system (Figs. 4(d) and (e)). After a period of waterdrop dripping, the superhydrophobic system could recover to the original state. However, a large amount of water remained on the hydrophilic system, allowing the magnetic top to adhere to the bottom. Figs. 4(c) and (f) show the continuous electrical responses of those two samples to 50 water droplets. There is a stable current response for the superhydrophobic 3DMD but an obvious damping in the output performance over time for the hydrophilic 3DMD.

The electrical output of the 3DMD, by virtue of the magnetic flux change, can be theoretically calculated due to Faraday's law of induction as follows [46]:

$$E = -n \cdot \frac{\Delta \Phi}{\Delta t} = -\sum_{i=1}^{n} \frac{\Delta \Phi_i}{\Delta t} = -\sum_{i=1}^{n} \frac{\Delta B_i \cdot S_i}{\Delta t} \quad (1)$$

where E is the output voltage, n is the turn number of the coil, $\Delta \Phi_i$ is the magnetic flux change through each equivalent coil ring, Δt is the response time of the 3DMD under deformation, ΔB_i is the magnetic intensity change of each equivalent ring, and S_i is the area of each equivalent coil ring.

Combined with Eq. (1), various fabrication parameters were investigated for their contribution to the electrical performance of the 3DMD, including the $Nd_2Fe_{14}B$ particle content, the papillary size, and the thickness of the magnetic top. For further study, only one variable parameter was tuned while the other fabrication and test parameters remained the same. An increase in the $Nd_2Fe_{14}B$ content from 20 wt% to 40 wt% leads to enhanced surface magnetic intensity (B) of the magnetic top, thereby remarkably improving the current output of the 3DMD (Fig. S7 in Appendix A). However, more magnetic fillers (> 40 wt%) could yield a higher magnetic strength but higher susceptible to a blockage issue in the FDM printer. Considering the trade-off between resolution and fluency in the printing process, the magnetic content was kept at 40 wt%. As shown in Fig. S8 in Appendix A, the size of the papillae on the magnetic top does not obviously affect the magnetic intensity or the electrical output. Additionally, magnetic tops of diverse thicknesses (1, 2, and 3 mm) were fabricated to adjust the magnetic intensity (Fig. S9 in Appendix A). Their 3D simulation calculations confirmed that the magnetic intensity increased with increasing magnetic thickness (Figs. S9(a)–(c) in Appendix A). Nevertheless, there is an obvious downwards trend in their current performance (Fig. S9(e) in Appendix A). Through a high-speed camera system, the small deformations of the same elastic stem were captured when a waterdrop fell onto the surface of the 3DMDs (Figs. S9(d) and (f) in Appendix A). Considering the weight of the magnetic top, a thinner top suggests more flexibility, enabling the elastic stem to deform more easily. Table S2 in Appendix A indeed shows a decrease in the magnetic flux change with increasing thickness of the magnetic top calculated by numerical simulations.

Moreover, we explored the stem length of the elastic bottom considering that it was deemed to play a key role in tuning the

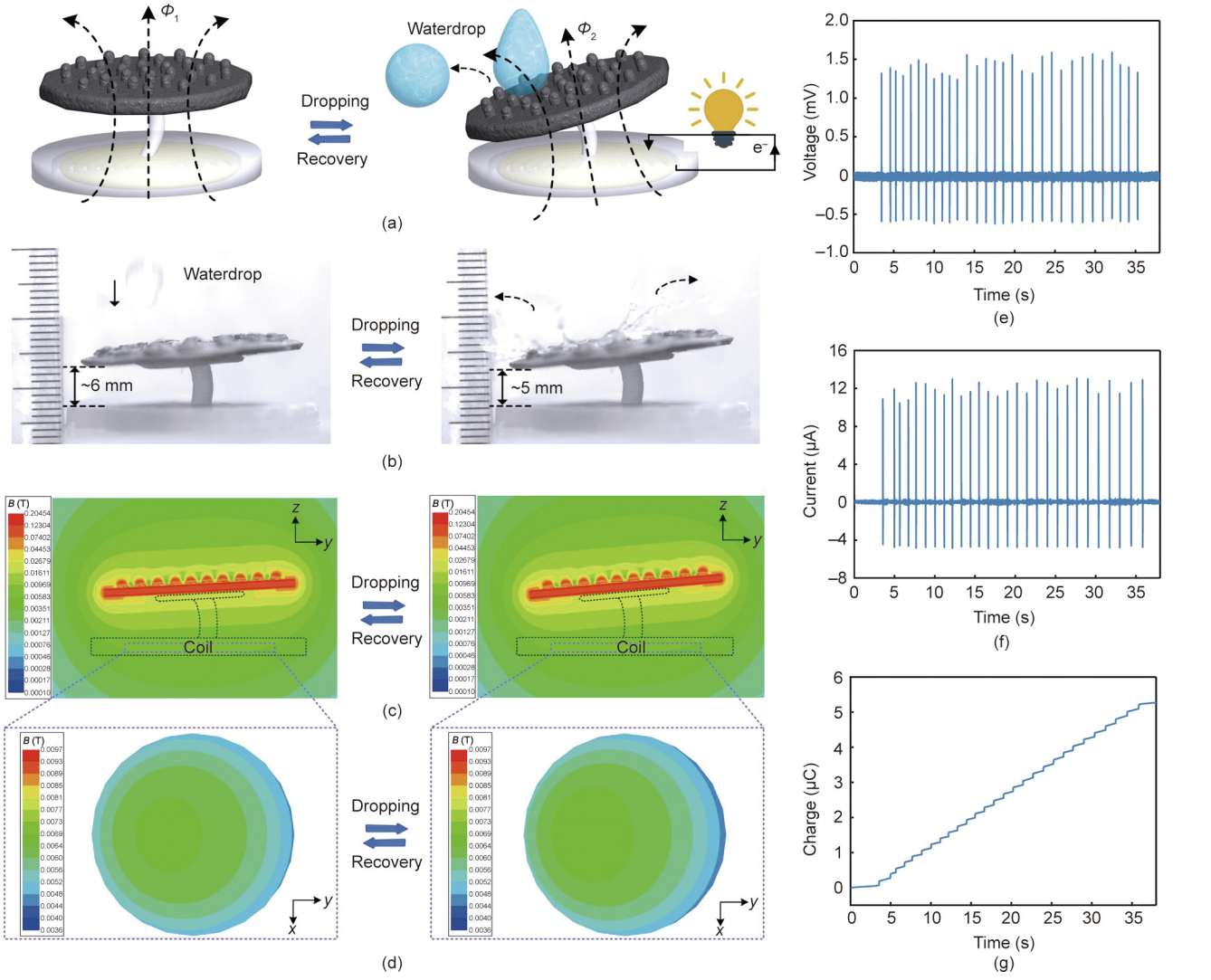

Fig. 3. The 3DMD exhibits a self-powered sensing capability for falling water droplets. (a) Schematic illustration of the mechanoelectrical conversion capacity of the 3DMD during waterdrop dripping; (b) optical images of the 3DMD before (left) and after (right) deformation due to waterdrop dripping captured by a high-speed camera system; obtained by 3D simulation calculations, (c) and (d) are 2D views of the magnetic intensity distribution of the 3DMD and the magnetic intensity through one turn of the coil before/after waterdrop dripping, respectively; the black and purple dotted lines in (c) present the positions of the elastic component and coil, respectively; corresponding electrical performance: (e) voltage output, (f) current output, and (g) transferred charge vs time curves. In this case, waterdrops (each droplet volume of 55 μL) were dripped onto the surface of the 3DMD with a release height of 40 cm. The magnetic content of the top is 40 wt%, and its thickness is 2 mm. Φ_1, Φ_2: the magnetic fluxes passing through the bottom coil before and after the waterdrop impact, respectively; B: magnetic strength.

Table 1
Comparison of different flexible tactile sensors.

Sensors	Sensing mechanism	Waterdrop response	Self-powered sensing	Output current (μA)	Ref.
Stretchable UV-curable hydrogel	Piezoresistive	N	N	N	[26]
Skin-like, hydrogel-based sensor	Capacitive	N	N	N	[27]
Fibre-based pressure sensor	Piezoelectric	N	√	0.15	[28]
Printable PDMS sensor	Triboelectric	N	√	8.40	[29]
Ultraflexible 3D sensor	Triboelectric	N	√	1.11	[30]
Bi-electrode freestanding generator	Triboelectric	√	√	0.54	[31]
Particle-laden droplet-driven generator	Triboelectric	√	√	1.50×10^{-4}	[32]
Superhydrophobic liquid–solid contact generator	Triboelectric	√	√	5.00×10^{-3}	[33]
Superhydrophobic generator	Triboelectric	√	√	4.50	[34]
FTCEs	Triboelectric	√	√	7.60	[35]
3DMD	Electromagnetic	√	√	12.56	This study

UV: ultraviolet; PDMS: polydimethylsiloxane; √: Yes; N: no; FTCEs: flexible transparent conducting electrodes.

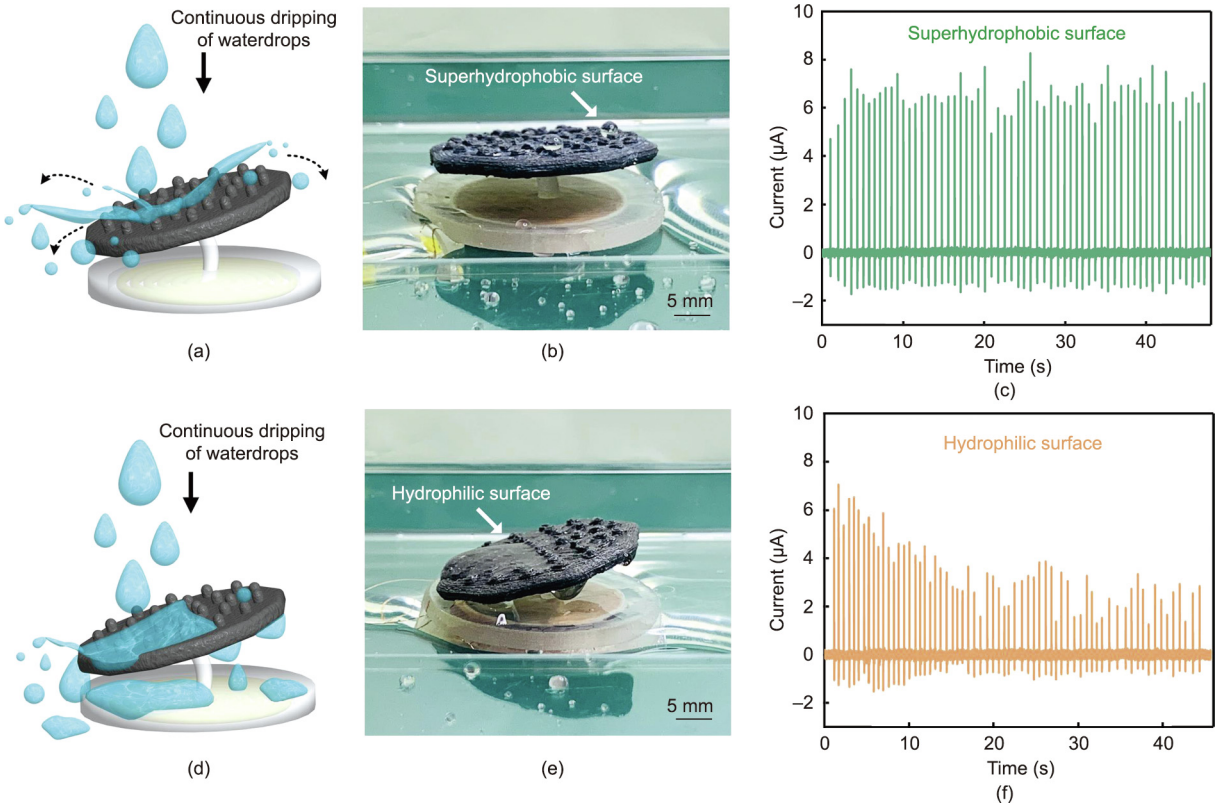

Fig. 4. Electrical performance of superhydrophobic and hydrophilic 3DMDs under continuous dripping of waterdrops. Schematic illustrations of continuous dripping of waterdrops for (a) superhydrophobic and (d) hydrophilic 3DMDs; (b) and (e) optical photographs of superhydrophobic and hydrophilic samples after 50 consecutive dripping cycles, respectively; (c) and (f) corresponding current responses over time.

gap between the magnetic top and the bottom coil. The other specifications were kept unchanged: the magnetic top was chosen to have the same thickness of 2 mm and magnetic content of 40 wt%. Four kinds of 3DMDs with different stem lengths ranging from 0.2 to 0.8 cm are shown in Figs. 5(a)–(c). When a water droplet dripped onto these 3DMDs under the same test parameters, their states before and after deformation were captured, as shown in Figs. 5(d)–(f). Combined with the snapshots in Fig. 3(b), an increase in the stem length contributes to slight improvement of the flexibility of 3DMD, yet there is no gradually enhanced output performance (Figs. 5(j) and (k)). The decline in the current output that appeared by varying the stem length from 0.6 to 0.8 cm was mainly attributed to the decreased magnetic intensity through one turn of the coil inside the 3DMD in the initial period and the corresponding decrease in the magnetic flux change (Fig. 3(d), Fig. 5(i), and Table 2). Thus, the stem length of 0.6 cm was deemed optimal for electrical response in this case.

The mechanoelectrical conversion capability of the 3DMD was further investigated. Even after waterdrops continually dripped for over 250 s, the mechanoelectrical conversion of the superhydrophobic 3DMD remained, showing its long-term stability (Figs. 6(a) and (b)). Furthermore, the as-fabricated 3DMD maintains a fair reliability after staying in the atmosphere for 28 days (Fig. S10 in Appendix A). Several test parameters, such as the water droplet volume, dripping height, and dripping rate, play an important role in the electrical output of the 3DMD. Increasing the volume or the dripping height of a waterdrop yields a larger gravitational potential energy, contributing to larger deformation between the magnetic and electrical components as well as enhanced mechanoelectrical conversion. The current peak value presents a nearly linear growth by varying the droplet volume from 26 to 55 μL, as shown in Figs. 6(c) and (d). Similarly, the current response significantly improves when the release height of a waterdrop is raised to 40 cm (Fig. S11 in Appendix A). Figs. 6(e) and (f) depict the correlation of the current performance and the dripping rate. Although an upwards trend in the output current was obtained as the dripping rate increased, the growth magnitude was quite small, with only a 2 μA increase under a rate change of more than 120 $\mu L \cdot s^{-1}$.

Considering the practical application in rainy weather, the 3DMD harvester can light up a commercial LED by using a stream of rainwater collected from a roof (Fig. 7(a)). A cluster-architecture setup was realized by integrating three 3DMDs in parallel. As shown in the inset image (Fig. 7(d)), the cluster-architecture setup was connected to a circuit system that consisted of amplifier and rectifier units and an LED. When a stream of water that simulated a rainy environment was released from a height of 40 cm onto the whole setup, a commercial red LED could be triggered to successfully light up (Fig. 7(b) and Movie S1 in Appendix A). This indicates that such a cluster-architecture setup converts the mechanical energy of the rainwater flow into electrical energy. In addition, the LED driven by the 3DMDs can potentially be applied as a pond/lake caution sign in remote environments to alert nearby persons to avoid falling on a rainy day. Fig. 7(c) records the current response of the setup within a period of 16 s. The corresponding accumulated charge during this process reached almost 40 μC (Fig. 7(d)).

4. Conclusions

We fabricated a flexible superhydrophobic and magnetic system for self-powered sensing of falling waterdrops by employing 3D printing. Two parts of the 3DMD, the magnetic top and the

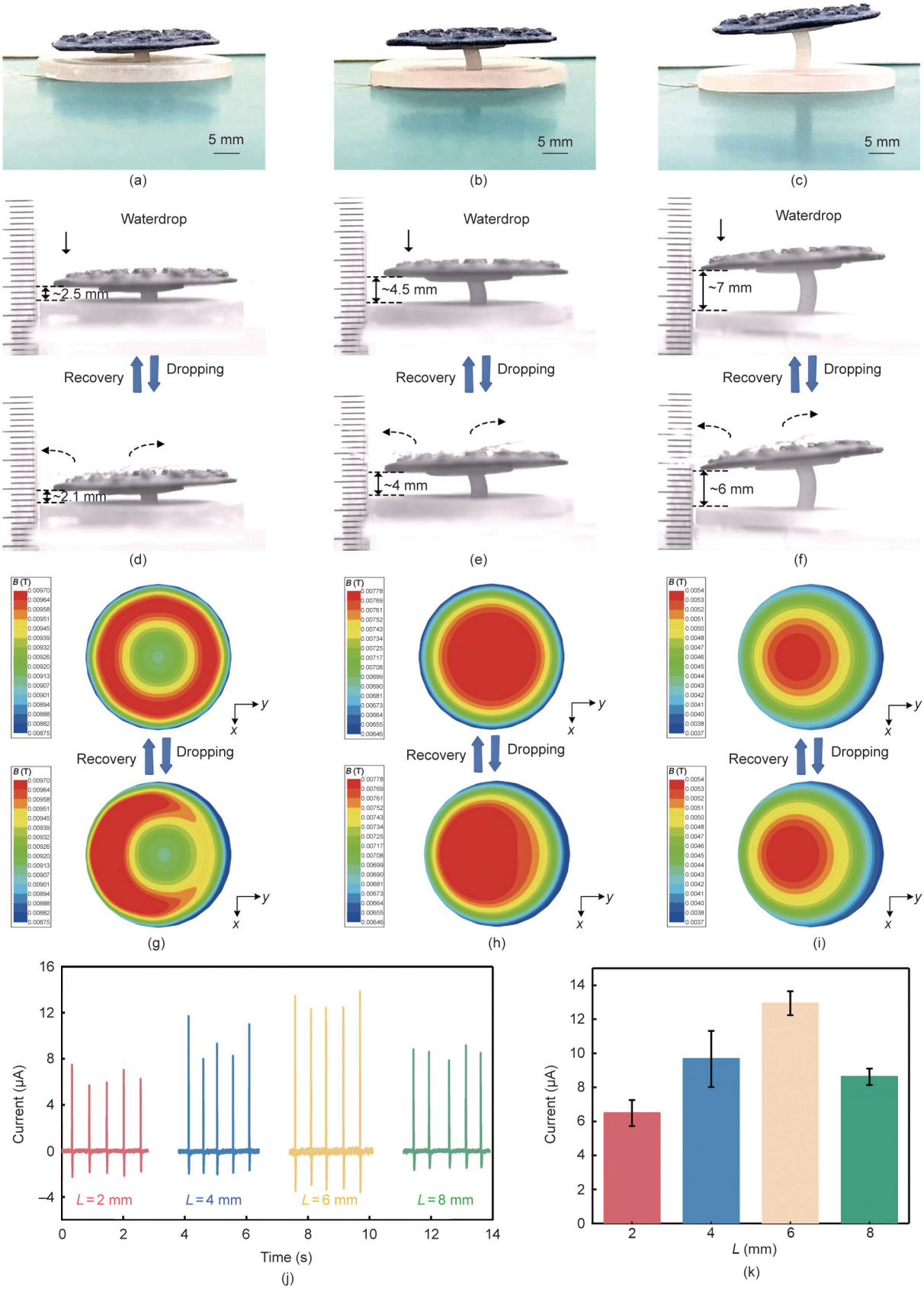

Fig. 5. Influence of the stem length of the elastic bottom on the electrical response of the 3DMD. Optical photographs of three kinds of 3DMDs with (a) 0.2 cm, (b) 0.4 cm, and (c) 0.8 cm elastic stems, their magnetic tops are the same with a 40 wt% magnetic loading and a thickness of 2 mm; (d), (e), and (f) snapshots of the three 3DMDs before/after deformation due to waterdrop dripping recorded by a camera system, the waterdrops were 55 μL, dropped from the same height of 40 cm; (g), (h), and (i) corresponding 3D-simulated distributions (*x*-*y* plane) of the magnetic intensity through an identical circle of the coil before/after waterdrop dripping; (j) current outputs of different 3DMDs with elastic stems of four lengths (*L*), and their comparison histogram is shown in (k).

Table 2
Calculated magnetic flux through one circle of the coil inside four different 3DMDs with different stem lengths of the elastic components before/after waterdrop dripping.

Stem length L (mm)	Φ_1 before dripping ($\times 10^{-6}$ Wb)	Φ_2 after dripping ($\times 10^{-6}$ Wb)	$\Delta\Phi$ ($\times 10^{-9}$ Wb)
2	4.946	4.949	2.64
4	3.875	3.879	3.36
6	3.095	3.106	10.30
8	2.503	2.511	8.27

$\Delta\Phi = \Phi_2 - \Phi_1$, where Φ_1 and Φ_2 represent the magnetic flux before and after dripping, respectively. The components of these four 3DMDs are the same except for the elastic stem-like support, and the chosen circles of the conductive coil for the simulated calculation have identical sizes.

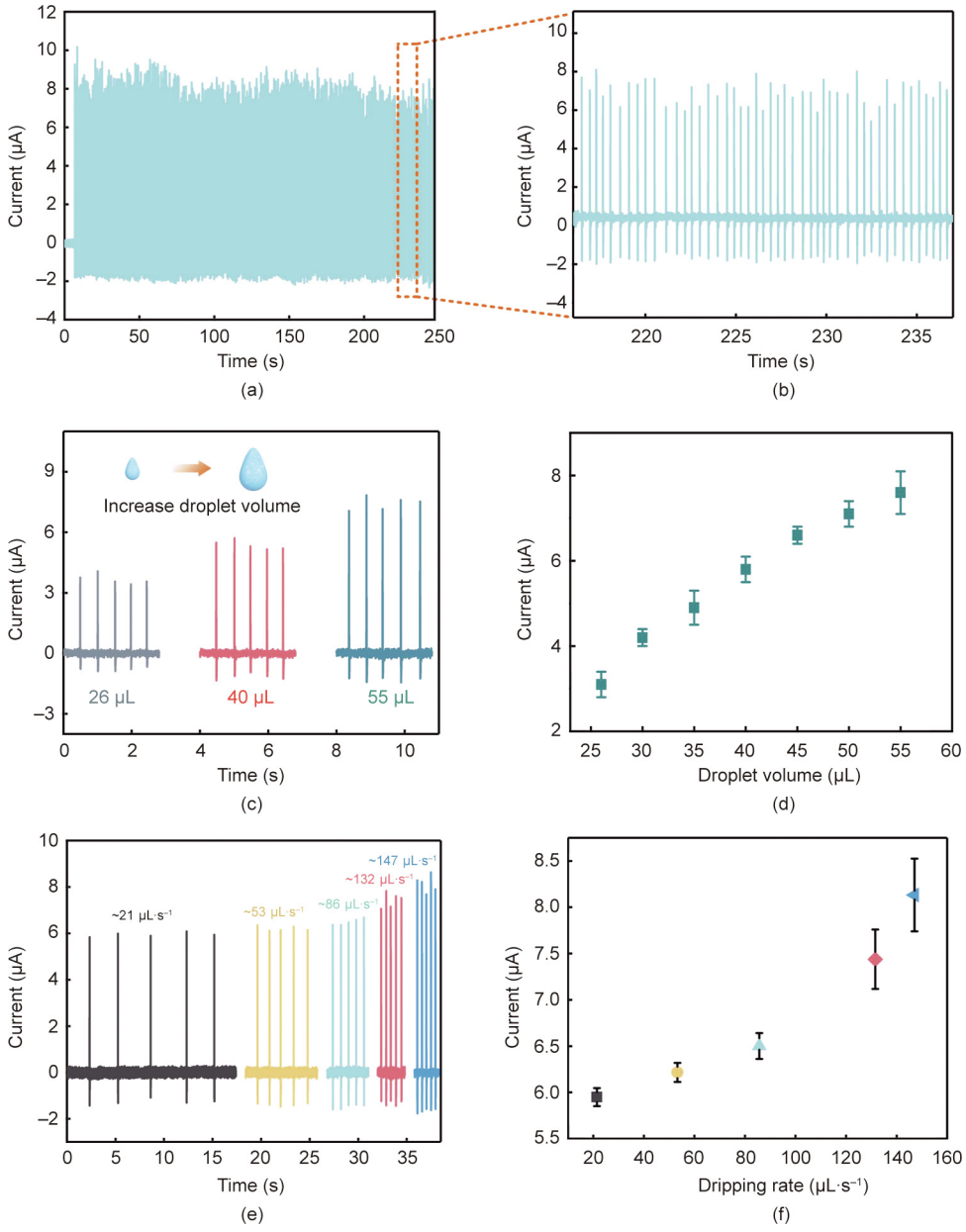

Fig. 6. Influence of diverse dripping parameters on the electrical response of the 3DMD. (a) Continuous test of waterdrop dripping for 250 s; (b) magnified diagram of (a), the 3DMD suffered from waterdrops continually dripped from a height of 40 cm; (c) current response to different volumes of water droplets dripping onto the 3DMD from the same height; (e) current outputs of the 3DMD when different waterdrop dripping rates were used; (d) and (f) statistical analysis of the output peaks from (c) and (e), respectively.

elastic stem-like bottom, were prepared by FDM and Polyjet techniques, respectively. Owing to the superhydrophobic surface, the 3DMD exhibits a long-term stable mechanoelectrical conversion capacity under consecutive water droplet dripping. This is mainly attributed to the effective reduction in solid/liquid adhesion that ensures a reliable distance change between the magnetic and

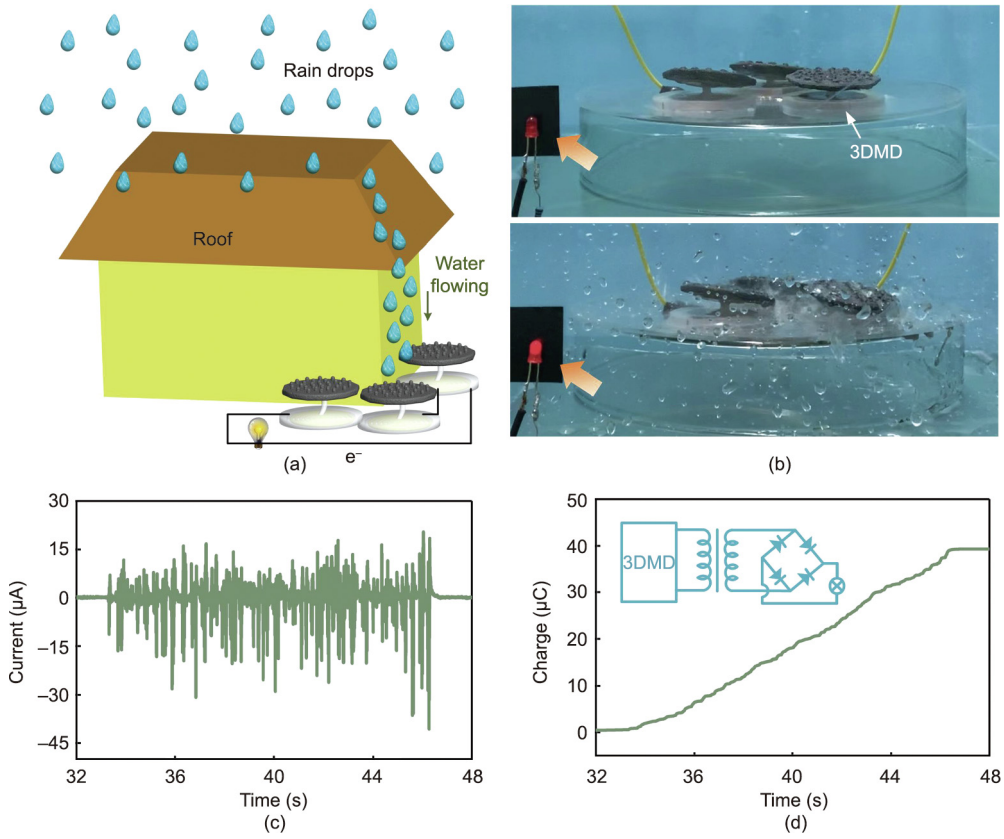

Fig. 7. Demonstration of the mechanoelectrical conversion of the whole setup based on a magnetic lotus-leaf cluster. (a) Schematic illustration of such a cluster-architecture magnetic setup integrating three 3DMDs in parallel driven by water flowing from a roof on a rainy day; (b) optical photographs of the cluster-architecture magnetic setup to trigger a commercial red LED when a stream of water falls onto the surface; (c) current response of the setup under flowing water; (d) transferred charge according to the current–time curve in (c). The inset shows a predesigned circuit diagram containing a voltage booster, as well as a rectifier.

electrical components, thereby realizing electricity generation. This study is believed to provide a new approach for flexible mechanoelectrical conversion strategies for raindrops and could be scaled up to vibration monitoring in the future [47].

Acknowledgments

This work was supported by initiatory financial support from Huazhong University of Science and Technology (HUST) and the Monash University Postgraduate Publications Award. The authors also gratefully acknowledge the guidance and help of group members of Simulation and Modelling of Particulate Systems (SIMPAS) and Australian Research Council (ARC) Research Hub for Computational Particle Technology.

Compliance with ethics guidelines

Xuan Zhang, Qi Wang, Ruiping Zou, Bo Song, Chunze Yan, Yusheng Shi, and Bin Su declare that they have no conflict of interest or financial conflicts to disclose.

Appendix A. Supplementary data

Supplementary data to this article can be found online at https://doi.org/10.1016/j.eng.2022.04.009.

References

[1] Kotz F, Risch P, Helmer D, Rapp BE. High-performance materials for 3D printing in chemical synthesis applications. Adv Mater 2019;31(26):1805982.
[2] Zarek M, Layani M, Cooperstein I, Sachyani E, Cohn D, Magdassi S. 3D printing of shape memory polymers for flexible electronic devices. Adv Mater 2016;28(22):4449–54.
[3] Yang Y, Li X, Zheng X, Chen Z, Zhou Q, Chen Y. 3D-printed biomimetic superhydrophobic structure for microdroplet manipulation and oil/water separation. Adv Mater 2018;30(9):1704912.
[4] Davoodi E, Fayazfar H, Liravi F, Jabari E, Toyserkani E. Drop-on-demand high-speed 3D printing of flexible milled carbon fiber/silicone composite sensors for wearable biomonitoring devices. Addit Manuf 2020;32:101016.
[5] Kalkal A, Kumar S, Kumar P, Pradhan R, Willander M, Packirisamy G, et al. Recent advances in 3D printing technologies for wearable (bio)sensors. Addit Manuf 2021;46:102088.
[6] Kolesky DB, Truby RL, Gladman AS, Busbee TA, Homan KA, Lewis JA. 3D bioprinting of vascularized, heterogeneous cell-laden tissue constructs. Adv Mater 2014;26(19):3124–30.
[7] Gul JZ, Sajid M, Rehman MM, Siddiqui GU, Shah I, Kim KH, et al. 3D printing for soft robotics—a review. Sci Technol Adv Mater 2018;19(1):243–62.
[8] Cooperstein I, Sachyani-Keneth E, Shukrun-Farrell E, Rosental T, Wang X, Kamyshny A, et al. Hybrid materials for functional 3D printing. Adv Mater Interfaces 2018;5(22):1800996.
[9] Podstawczyk D, Nizioł M, Szymczyk P, Wiśniewski P, Guiseppi-Elie A. 3D printed stimuli-responsive magnetic nanoparticle embedded alginate-methylcellulose hydrogel actuators. Addit Manuf 2020;34:101275.
[10] Chin SY, Poh YC, Kohler AC, Compton JT, Hsu LL, Lau KM, et al. Additive manufacturing of hydrogel-based materials for next-generation implantable medical devices. Sci Rob 2017;2(2):eaah6451.
[11] Marco C, Alcântara CCJ, Kim S, Briatico F, Kadioglu A, Bernardis G, et al. Indirect 3D and 4D printing of soft robotic microstructures. Adv Mater Technol 2019;4(9):1900332.
[12] Zhang J, Zhao S, Zhu M, Zhu Y, Zhang Y, Liu Z, et al. 3D-printed magnetic Fe3O4/MBG/PCL composite scaffolds with multifunctionality of bone regeneration, local anticancer drug delivery and hyperthermia. J Mater Chem B 2014;2(43):7583–95.
[13] Kokkinis D, Schaffner M, Studart AR. Multimaterial magnetically assisted 3D printing of composite materials. Nat Commun 2015;6:8643.
[14] Huber C, Abert C, Bruckner F, Groenefeld M, Muthsam O, Schuschnigg S, et al. 3D print of polymer bonded rare-earth magnets, and 3D magnetic field scanning with an end-user 3D printer. Appl Phys Lett 2016;109(16):162401.
[15] Martin JJ, Fiore BE, Erb RM. Designing bioinspired composite reinforcement architectures via 3D magnetic printing. Nat Commun 2015;6:8641.

[16] Ji Z, Yan C, Yu B, Wang X, Zhou F. Multimaterials 3D printing for free assembly manufacturing of magnetic driving soft actuator. Adv Mater Interfaces 2017;4(22):1700629.
[17] Kim Y, Yuk H, Zhao R, Chester SA, Zhao X. Printing ferromagnetic domains for untethered fast-transforming soft materials. Nature 2018;558(7709):274–9.
[18] Qi S, Guo H, Fu J, Xie Y, Zhu M, Yu M. 3D printed shape-programmable magneto-active soft matter for biomimetic applications. Compos Sci Technol 2020;188:107973.
[19] Wu H, Wang O, Tian Y, Wang M, Su B, Yan C, et al. Selective laser sintering-based 4D printing of magnetism-responsive grippers. ACS Appl Mater Interfaces 2021;13(11):12679–88.
[20] Ma Z, Ai J, Shi Y, Wang K, Su B. A superhydrophobic droplet-based magnetoelectric hybrid system to generate electricity and collect water simultaneously. Adv Mater 2020;32(50):2006839.
[21] Zhang X, Ai J, Ma Z, Du Z, Chen D, Zou R, et al. Magnetoelectric soft composites with a self-powered tactile sensing capacity. Nano Energy 2020;69:104391.
[22] Zhang X, Ai J, Zou R, Su B. Compressible and stretchable magnetoelectric sensors based on liquid metals for highly sensitive, self-powered respiratory monitoring. ACS Appl Mater Interfaces 2021;13(13):15727–37.
[23] Hong H, Wei J, Yuan Y, Chen FP, Wang J, Qu X, et al. A novel composite coupled hardness with flexibleness—polylactic acid toughen with thermoplastic polyurethane. J Appl Polym Sci 2011;121(2):855–61.
[24] Boyacioglu S, Kodal M, Ozkoc G. A comprehensive study on shape memory behavior of PEG plasticized PLA/TPU bio-blends. Eur Polym J 2020;122:109372.
[25] Wu C, Do TT, Tran P. Mechanical properties of PolyJet 3D-printed composites inspired by space-filling peano curves. Polymers 2021;13(20):3516.
[26] Zhang B, Li S, Hingorani H, Serjouei A, Larush L, Pawar AA, et al. Highly stretchable hydrogels for UV curing based high-resolution multimaterial 3D printing. J Mater Chem B 2018;6(20):3246–53.
[27] Lei Z, Wang Q, Wu P. A multifunctional skin-like sensor based on a 3D printed thermo-responsive hydrogel. Mater Horiz 2017;4(4):694–700.
[28] Fuh YK, Wang BS, Tsai CY. Self-powered pressure sensor with fully encapsulated 3D printed wavy substrate and highly-aligned piezoelectric fibers array. Sci Rep 2017;7:6759.
[29] Haque RI, Chandran O, Lani S, Briand D. Self-powered triboelectric touch sensor made of 3D printed materials. Nano Energy 2018;52:54–62.
[30] Chen B, Tang W, Jiang T, Zhu L, Chen X, He C, et al. Three-dimensional ultraflexible triboelectric nanogenerator made by 3D printing. Nano Energy 2018;45:380–9.
[31] Zhao L, Liu L, Yang X, Hong H, Yang Q, Wang J, et al. Cumulative charging behavior of water droplet driven freestanding triboelectric nanogenerators toward hydrodynamic energy harvesting. J Mater Chem A 2020;8(16):7880–8.
[32] Yang L, Wang Y, Zhao Z, Guo Y, Chen S, Zhang W, et al. Particle-laden droplet-driven triboelectric nanogenerator for real-time sediment monitoring using a deep learning method. ACS Appl Mater Interfaces 2020;12(34):38192–201.
[33] Hu S, Shi Z, Zheng R, Ye W, Gao X, Zhao W, et al. Superhydrophobic liquid–solid contact triboelectric nanogenerator as a droplet sensor for biomedical applications. ACS Appl Mater Interfaces 2020;12(36):40021–30.
[34] Niu J, Xu W, Tian K, He G, Huang Z, Wang Q. Triboelectric energy harvesting of the superhydrophobic coating from dropping water. Polymers 2020;12(9):1936.
[35] Zhou Q, Park JG, Kim KN, Thokchom AK, Bae J, Baik JM, et al. Transparent–flexible–multimodal triboelectric nanogenerators for mechanical energy harvesting and self-powered sensor applications. Nano Energy 2018;48:471–80.
[36] Su Y, Wen X, Zhu G, Yang J, Chen J, Bai P, et al. Hybrid triboelectric nanogenerator for harvesting water wave energy and as a self-powered distress signal emitter. Nano Energy 2014;9:186–95.
[37] Su Y, Xie G, Tai H, Li S, Yang B, Wang S, et al. Self-powered room temperature NO_2 detection driven by triboelectric nanogenerator under UV illumination. Nano Energy 2018;47:316–24.
[38] Wang S, Jiang Y, Tai H, Liu B, Duan Z, Yuan Z, et al. An integrated flexible self-powered wearable respiration sensor. Nano Energy 2019;63:103829.
[39] Su Y, Wang J, Wang B, Yang T, Yang B, Xie G, et al. Alveolus-inspired active membrane sensors for self-powered wearable chemical sensing and breath analysis. ACS Nano 2020;14(5):6067–75.
[40] Su Y, Chen C, Pan H, Yang Y, Chen G, Zhao X, et al. Muscle fibers inspired high-performance piezoelectric textiles for wearable physiological monitoring. Adv Funct Mater 2021;31(19):2010962.
[41] Su Y, Chen G, Chen C, Gong Q, Xie G, Yao M, et al. Self-powered respiration monitoring enabled by a triboelectric nanogenerator. Adv Mater 2021;33(35):2101262.
[42] Su Y, Yang T, Zhao X, Cai Z, Chen G, Yao M, et al. A wireless energy transmission enabled wearable active acetone biosensor for non-invasive prediabetes diagnosis. Nano Energy 2020;74:104941.
[43] Su Y, Li W, Yuan L, Chen C, Pan H, Xie G, et al. Piezoelectric fiber composites with polydopamine interfacial layer for self-powered wearable biomonitoring. Nano Energy 2021;89:106321.
[44] Kong T, Luo G, Zhao Y, Liu Z. Bioinspired superwettability micro/nanoarchitectures: fabrications and applications. Adv Funct Mater 2019;29(11):1808012.
[45] Shi J, Wang L, Dai Z, Zhao L, Du M, Li H, et al. Multiscale hierarchical design of a flexible piezoresistive pressure sensor with high sensitivity and wide linearity range. Small 2018;14(27):1800819.
[46] Guru BS, Hiziroğlu HR. Electromagnetic field theory fundamentals. Cambridge: Cambridge University Press; 2005.
[47] Zhou Y, Zhao X, Xu J, Fang Y, Chen G, Song Y, et al. Giant magnetoelastic effect in soft systems for bioelectronics. Nat Mater 2021;20(12):1670–6.